Research Article

Kittipong Kunchariyakun, Suthatip Sinyoung*, Kenneth J. D. MacKenzie, Vithit Pungkun, Pakkamai Raknarong, Musofpar Teh, Afham Jekabaso, and Narumol Sittichan

Experimental study of mortar incorporating nano-magnetite on engineering performance and radiation shielding

https://doi.org/10.1515/ntrev-2024-0135
received March 24, 2024; accepted December 10, 2024

Abstract: Here, this study reports the effect of nano-magnetite (nano-Fe_3O_4) on the γ and neutron-radiation shielding properties of mortar using 1–10 wt% additions of nano-Fe_3O_4. The results indicate that nano-Fe_3O_4 additions enhance the radiation-shielding properties of the mortar as a result of pore filling and nucleation effects. The mortar incorporating nano-Fe_3O_4 exhibited relatively high compressive strength values at 28 and 90 days compared to the control mixture (NFC0). A 5 wt% addition of nano-Fe_3O_4 provided the best physical (1,847 ± 19.1 kg m^{-3}), compressive strength (216.79 ± 6.19 ksc at 28 days), and radiation shielding properties, increasing the photon linear attenuation coefficient to 0.155 cm^{-1} from 0.144 cm^{-1} in the material without nano-Fe_3O_4. This 5 wt% addition of nano-Fe_3O_4 also increased fast neutron removal cross-section (Σ_R) of neutrons from 0.1109 cm^{-1} in the control sample to 0.1192 cm^{-1}. These results indicate that the addition of nano-Fe_3O_4 to radiation-shielding mortar can potentially attenuate gamma rays rather than neutrons and lead to the development of materials for shielding radiation from radioactive storage facilities, thereby reducing the impact of this hazardous waste on humans and the environment.

Keywords: nano-magnetite, radiation shielding, mortar, compressive strength, microstructure

1 Introduction

Nowadays, nuclear materials are widely used in various applications such as medical diagnostics, nuclear research, nuclear reactors, and high-energy particle accelerators. All these activities eventually involve the need to store radioactive waste and protect the living from the natural radioelements [1–3], ideally in ways that decrease the effect of nuclear radiation. For this purpose, a number of shielding materials have been investigated, for example, building materials [4,5], polymers [6], and glass [7]. Cementitious materials, which can also include the incorporation of waste materials, have proved to be extremely popular for this application because of their ease and flexible construction method [8–11], their relative cheapness, and their ability to provide a high shielding capacity for nuclear radiation. Typically, high-density concrete (approximately 2,600–4,500 kg m^{-3}) is specified for radiation shielding because of its excellent gamma-ray attenuation and the fact that the presence of hydrogenous materials, heavy metal elements, and other neutron absorbers in its matrix [12] will improve its ability to shield against neutrons.

From the previous literature [13–19], radiation shielding concrete (RSC) is a useful material by virtue of its good shielding ability, high durability, low cost, and good versatility, providing it with structural functionality that outperforms design standards [18]. More than 60% of light water reactor nuclear power plants in the United States are constructed using RSC [18]. In addition, radiation-shielding concrete is used as biological shielding in nuclear power plants,

* **Corresponding author: Suthatip Sinyoung,** Department of Civil and Environmental Engineering, Faculty of Engineering, Prince of Songkla University, Songkhla, Thailand, e-mail: ssuthatip@eng.psu.ac.th, suthatip.sin@gmail.com, tel: +66-74-287124
Kittipong Kunchariyakun: School of Engineering and Technology, Walailak University, Nakhonsithammarat, Thailand; Center of Excellence in Sustainable Disaster Management, Walailak University, Nakhonsithammarat, Thailand
Kenneth J. D. MacKenzie: MacDiarmid Institute for Advanced Materials and Nanotechnology, School of Chemical and Physical Science, Victoria University of Wellington, Wellington, New Zealand
Vithit Pungkun: Ionising Radiation Metrology Section, Regulatory Technical Support Division, Office of Atoms for Peace, Bangkok, Thailand
Pakkamai Raknarong, Musofpar Teh, Afham Jekabaso, Narumol Sittichan: School of Engineering and Technology, Walailak University, Nakhonsithammarat, Thailand

particle accelerators, medical units, and radioactive waste storage facilities [19]. In the world's oldest nuclear industry (in the UK), about 4.9 million tons of radioactive waste is forecast to be produced by 2125 [20]. Therefore, there will be an ongoing necessity for the development of radiation shielding material to reduce the impact of nuclear radiation on living organisms and the environment.

With the advent of nanotechnology, extensive research has been carried out in the past decade into the applications of nanomaterials in various fields, including cementitious materials. The effect on the properties of cementitious materials of various nanomaterials such as nano-silica [21–23], carbon nanotubes [24], nano-titanium [25,26], nano-aluminum [27], and nano-Fe_2O_3 [28,29] has been reported. Of these nanomaterials, nano-silica had the most beneficial effect on cementitious materials due to its pozzolanic properties [30], but more recently, nano-magnetite (nano-Fe_3O_4) has been of interest as a nano-additive. Amin *et al.* [31] showed that a small addition of nano-Fe_3O_4 (up to 0.3%) can enhance the mechanical properties of cement and refine its pore structure. Sikora *et al.* [32] reported that cementitious composites containing nano-Fe_3O_4 showed an improvement in the compressive strength of up to 20%, while Bragança *et al.* [33] examined the effect of chloride and sulfate conditions on concrete containing 1% nano-Fe_3O_4 and concluded that the addition of nano-Fe_3O_4 produced a more durable cement matrix even in such highly aggressive environments. An improvement in the thermal resistance of cementitious materials containing nano-Fe_3O_4 at temperatures up to 600°C has also been reported [19].

An examination of the literature suggests that the addition of nano-Fe_3O_4 to cementitious materials is likely to result in a reduction in the porosity of the cement, leading to a higher relative density. This effect could be the key to the development of high-density concrete for gamma-ray attenuation [34]. Horszczaruk *et al.* [35] noted that the gamma-ray attenuation coefficient of cement pastes increased with increasing density caused by the incorporation of nano-Fe_3O_4. Florez *et al.* [36] also reported that the addition of nano-Fe_3O_4 in the cement paste enhanced both the compressive strength and the gamma-ray attenuation coefficient. However, the literature on the effect of cementitious materials containing nano-Fe_3O_4 on neutron attenuation is limited. In the present investigation, the effect of adding various percentages (1–10 wt%) of nano-Fe_3O_4 to mortar for radiation shielding applications was determined by studying the physical and mechanical properties as well as the microstructures of the materials and their efficiency in shielding both gamma-rays and neutrons.

2 Methodology

2.1 Materials and mix proportions

The starting materials in this study were ordinary Portland cement (OPC), river sand, water, and nano-magnetite (nano-Fe_3O_4). The specific gravity of the OPC was 3.13, and its chemical composition is presented in Table 1. The river sand had a fineness modulus of 2.58 and a specific gravity of 2.65. The nano-Fe_3O_4 (carbon nanotube materials store, CAS No. 1317-61-9) had a purity of 96.42% (Table 1) with a particle size of 50–100 nm (Figure 1a) and was characterized by Brunauer–Emmett–Teller (BET) (Micromeritics – ASAP2460), transmission electron microscopy (TEM) (JEM 2010), X-ray fluorescence (XRF) (Philips PW2400 XRF spectrometer), and X-Ray diffraction analysis (XRD) (Rigaku Miniflex 600 with Cu Kα radiation, λ = 1.5406 Å, 40 kV and 40 mA). The BET surface area of the nano-Fe_3O_4 was 12.763 $m^2\ g^{-1}$, with a total pore volume of 0.0454 $cm^3\ g^{-1}$ and an average pore diameter of 142.283 Å. The TEM micrograph (Figure 1a) shows the particles to be predominantly spherical, while the XRD of this phase (Figure 1b) contains the reflections of crystalline magnetite (ICDD database no. 01-088-0866).

2.2 Experimental program

2.2.1 Sample preparation

The samples, containing OPC, river, sand, and nano-Fe_3O_4, were weighed and dry-mixed in a Hobart mixer for 1 min.

Table 1: Chemical composition of the starting materials OPC, sand, and nano-Fe_3O_4

Compounds	Concentration (%)		
	OPC	Nano-Fe_3O_4	Sand
CaO	70.1	0.04	—
SiO_2	15.2	0.49	96.21
Fe_2O_3	3.29	—	0.04
Fe_3O_4	—	96.42	—
Al_2O_3	3.33	0.01	6.21
MgO	1.89	0.97	—
Na_2O	—	0.18	0.56
P_2O_5	0.03	0.01	—
SO_3	4.39	0.45	—
Cl	0.02	0.02	—
TiO_2	0.21	0.12	0.05
MnO	0.03	0.73	—
ZnO	0.01	0.04	—
K_2O	1.30	—	0.54
SrO	0.07	—	—
H_2O	—	—	—

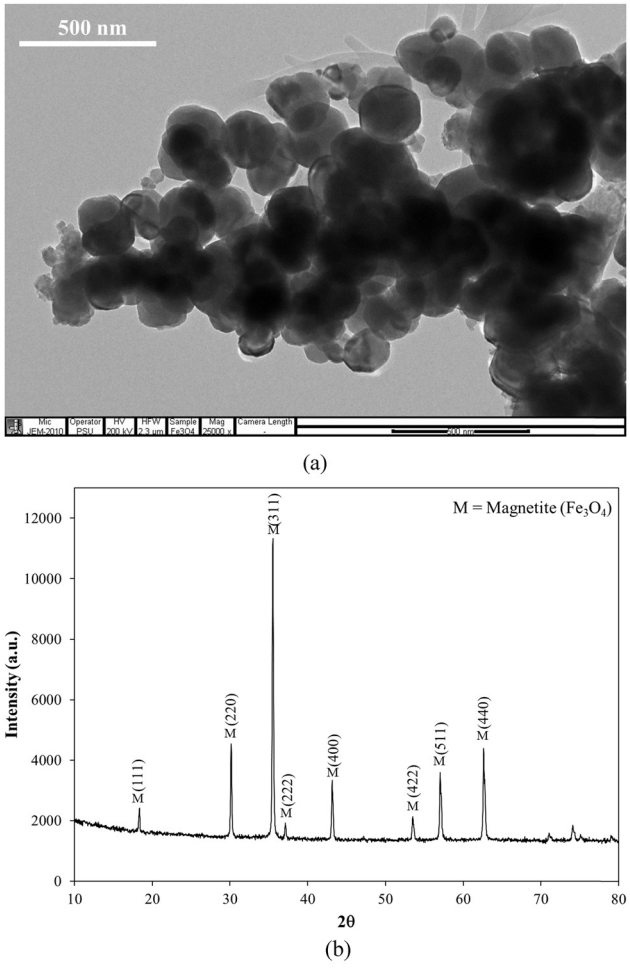

Figure 1: Characteristics of the nano-Fe_3O_4: (a) TEM micrograph and (b) XRD diffractogram.

The compositions of the samples containing 1, 3, 5, 7, and 10% nano-Fe_3O_4 by weight of OPC (designated NFC1, NFC3, NFC5, NFC7, and NFC10, respectively) and a control sample without nano-Fe_3O_4 (NFC0) are shown in Table 1. The preparation process of the samples is illustrated in Figure 2. Water was added to these dry mixtures before mixing again for 1.5 min. The slurry was then poured into 5 × 5 × 5 cm^3 molds for the measurements of dry density, water absorption, and compressive strength according to ASTM C109 [37]. In addition, 30 × 30 cm^2 molds of thicknesses ranging from 2 to 8 cm were prepared for tests of radiation transmission. After casting, the samples remained in the molds overnight before demolding and curing for 7, 28, and 90 days for compressive strength determinations using a compression testing machine, 28 days for measurements of the dry density and water absorption, and 90 days for the radiation transmission tests.

2.2.2 Radiation transmission tests

The representative samples chosen for these attenuation measurements were samples NFC0, NFC5, and NFC10. Prior to testing, the cured samples were dried in an electric oven at 105°C. A 0.662 MeV Cs^{137} gamma-ray source with 0.662 MeV was used, with a NaI (TI) scintillation detector and a multi-channel analyzer. The neutron cross-section measurements were made using a 241 Am–Be neutron-sealed source and a BF3 detector. Figure 3 shows the schematic diagram for the gamma-ray attenuation and neutron cross-section measurements.

The transmitted radiation intensity I was calculated by the Beer–Lambert law,

$$I = I_0 e^{-\mu x}, \quad (1)$$

where I is the radiation intensity passing through the samples of different thicknesses (compared to the source intensity I_0), x is the sample thickness (cm), and μ is the linear attenuation coefficient for gamma rays. The equation for the fast removal cross-section for neutrons (Σ_R) (cm^{-1}) is also applied from equation (1), which changes from μ to Σ_R.

Then, the total mass attenuation coefficients (μ_m) were calculated by

$$\mu_m = \mu/\rho, \quad (2)$$

where ρ is the sample density.

Figure 2: Samples preparation process.

The radiation shielding potential of a material can also be reported as the half-value layer (HVL) and tenth-value layer (TVL), which refers to the thickness of the samples that reduces the radiation intensity to half or one-tenth of its original intensity. The HVL and TVL values can be expressed as

$$\text{HVL} = \ln 2/\mu, \tag{3}$$

$$\text{TVL} = \ln 10/\mu. \tag{4}$$

The mean free path (mfp), which is the average distance between two successive interactions of photons, can be calculated by

$$\text{mfp} = 1/\mu. \tag{5}$$

2.2.3 Microstructure analysis

The microstructures of the samples were investigated by XRD (Rigaku Miniflex 600 with Cu Kα radiation, λ = 1.5406 Å, 40 kV, and 40 mA), Fourier transform infrared spectroscopy (Bruker Tensor 27 FTIR spectrometer), and scanning electron microscopy (JEOL-JSM-6400, 10 kV). The samples of NFC0, NFC5, and NFC10 were also selected to represent the behavior of this investigation. The SEM analysis was carried out with the morphology changed by adding nano-Fe_3O_4 and was prepared by broken samples from compressive strength testing, which were soaked in acetone to remove any remaining water and then gold-coated. The samples (broken compressive strength test samples) for XRD and FTIR analyses were prepared by grinding and soaking the samples in acetone. The FTIR was carried out on the functional groups that had changed due to the addition of nano-Fe_3O_4. The crystalline phases that had changed under curing times (7–90 days) and the nano-Fe_3O_4 contents were observed by XRD. The XRD diffraction patterns were obtained with a step size of 0.02° in the range 10°–60° 2θ at a scan rate of 3° min^{-1}. The FTIR samples were packed in a circle sheet and scanned with an attenuated total reflection (ATR) method in the range 400–4,000 cm^{-1} with a resolution of 4 cm^{-1}.

3 Results

3.1 Compressive strength

The compressive strength measurements of the samples after 7, 28, and 90 days (Figure 4) show that the strength increased with increasing nano-Fe_3O_4 content up to 5% by weight (sample NFC5), but then continuously declined at all curing times with further additions of nano-Fe_3O_4. The nano-Fe_3O_4 acted as a filler and nucleating agent, resulting in the formation of denser and more compact microstructures [32,38,39]. However, the reduction in the compressive strength in the samples containing more than the optimum 5% by weight of nano-Fe_3O_4 may be due to two reasons:

(1) The presence of the additional nanoparticles decreases the available space for the growth of crystalline calcium hydroxide (portlandite) crystals, thereby decreasing the ratio of the crystals to the strengthening gel. This would lead to an increase in both the shrinkage and creep in the cement paste, which would become more porous [38].
(2) Another possible explanation might be the agglomeration of the nano-Fe_3O_4, decreasing its ability to actively participate in the hydration process [32].

An interesting feature of this study is the relatively high compressive strengths of samples NFC7 and NFC10 compared to the control sample NFC0. These results are attributed to the beneficial effect of high nano-Fe_3O_4 contents on strength development in the samples. It should also be noted that the optimum nano-Fe_3O_4 content of the present study (5%) is consistent with a previous literature report [40]. In addition, at this nano-Fe_3O_4 content (5%), a relatively high strength development from 28 to 90 days (approximately 11%) was shown, compared to the NFC0 sample (5%). This was possibly due to the nano-Fe_3O_4 reacting with the remaining $Ca(OH)_2$, resulting in

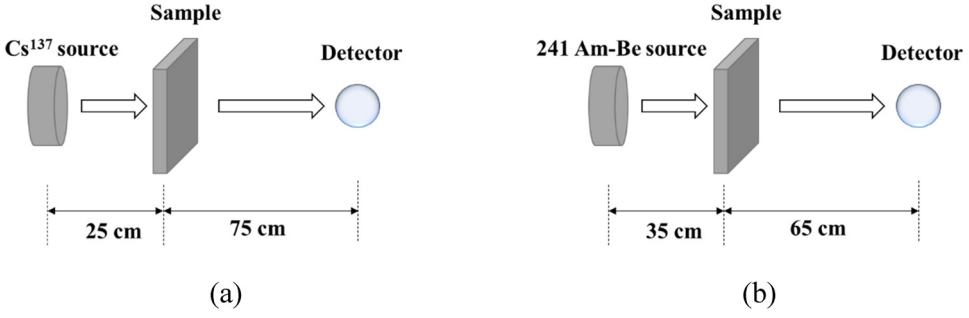

Figure 3: Schematic diagrams of (a) the gamma-ray attenuation measurement and (b) the neutron cross-section measurement.

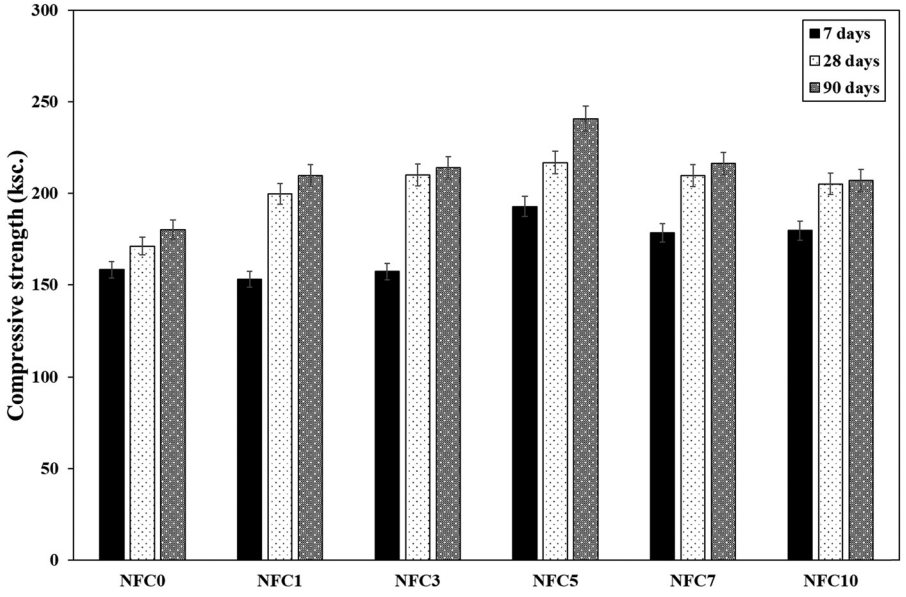

Figure 4: Compressive strengths of the magnetite/mortar samples and the control sample at 7, 28, and 90 days.

nucleating and facilitating the C–S–H or other hydrate phase formations [33].

3.2 Dry density and water absorption

The 28-day dry density values of the present samples (Figure 5, solid bars) behave similarly to their compressive strengths (Figure 4), increasing with increasing nano-Fe_3O_4 contents up to 5%, but decreasing at higher nano-Fe_3O_4 contents. The relatively low dry density of the mortar containing nano-Fe_3O_4 of more than 5% was due to the loose porous structure in the matrix caused by agglomeration or the amount of nano-Fe_3O_4. The dry density values were 1,733, 1,729, 1,794, 1,847, 1,771, and 1,758 kg m^{-3} for NFC0–NFC10, respectively. The values also exhibited that the addition of nano-Fe_3O_4 tends to gain high dry density, compared to samples without nano-Fe_3O_4. The relatively high density of NFC came from the refinement pore structure in the mortar matrix [31] and the high density of the Fe_3O_4 nanoparticles [38].

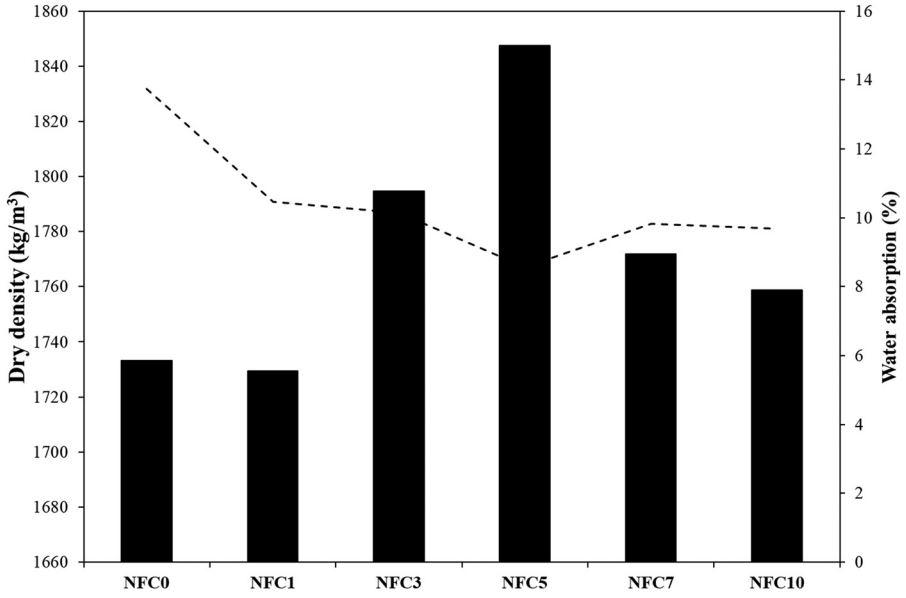

Figure 5: Dry density and water absorption results at 28 days.

The water absorption of the samples containing nano-Fe_3O_4 (Figure 5, broken line) indicates that the addition of nano-Fe_3O_4 produces a less porous, denser structure of the mortar matrix. Previous studies [40,41] have similarly shown that nanoparticles can occupy the voids and pores in a cement matrix, leading to improved particle packing and reduced water absorption. The loss of absorption water values from the control sample (NFC0) and the samples containing nano-Fe_3O_4, calculated from the water absorption values, are 23, 26, 37, 28, and 29% for NFC1, NFC3, NFC5, NFC7, and NFC10, respectively.

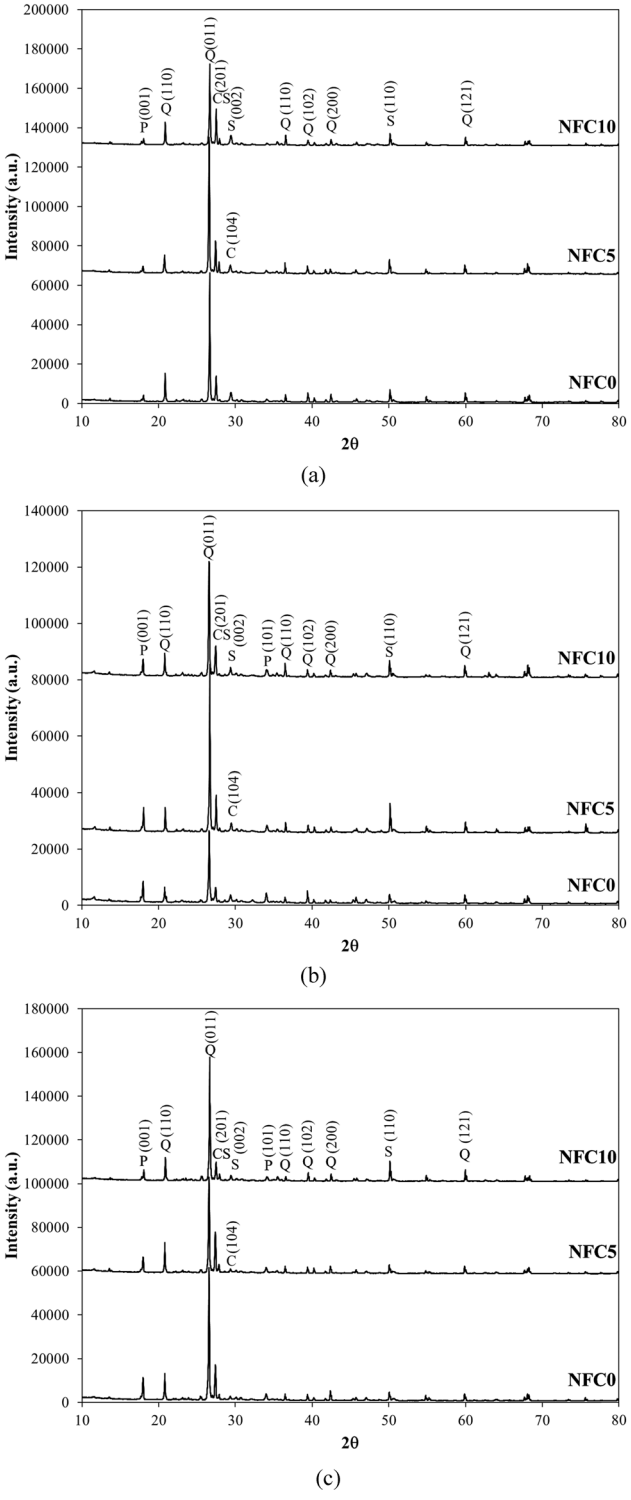

Figure 6: XRD patterns of selected magnetite/mortar samples and the control sample at (a) 7 days, (b) 28 days, and (c) 90 days. Key: Q = Quartz, C = calcite, P = Portlandite, S = calcium silicate hydrate, and CS = calcium silicate.

3.3 Microstructure

The microstructure analyses were carried out on samples NFC0, NFC5, and NFC10. The XRD diffractograms patterns of all the 7-day samples (Figure 6a) contain the reflections of quartz (ICDD database no. 01-070-7344), calcite (ICDD database no. 01-083-0577), portlandite ($Ca(OH)_2$, ICDD database no. 00-044-1481), calcium silicate hydrate (C–S–H, ICDD database no. 00-33-0306), and calcium silicate (ICDD database no. 00-027-1064). These peaks also occur in the 28 and 90-day samples (Figure 6b and c). However, the portlandite peaks at ≈18° and 34° 2θ in the samples cured for 28 days are of slightly higher relative intensity (Figure 6b); portlandite is known to be one of the products of the hydration process, especially the reaction of the calcium silicates (C_2S and C_3S) with water [42,43]. Thus, the portlandite is probably related to the matrix C–S–H and thus to the development of 28-day compressive strength. Interestingly, the intensity of the portlandite peak at 18° 2θ in the 90-day samples containing nano-Fe_3O_4 decreases (Figure 6c), possibly due to the formation of further hydration products by the reaction of the portlandite with nano-Fe_3O_4 at longer curing times.

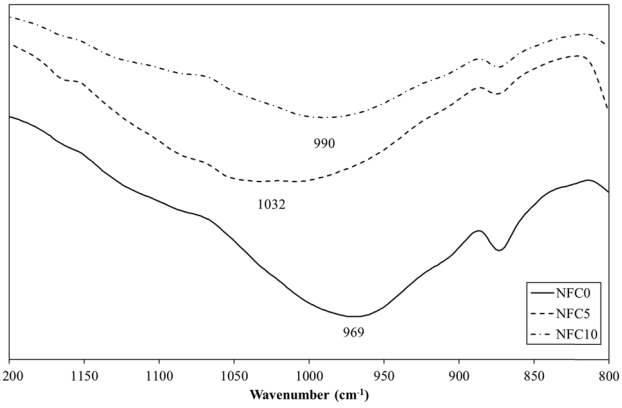

Figure 7: FTIR spectra of the 28-day samples and the control sample.

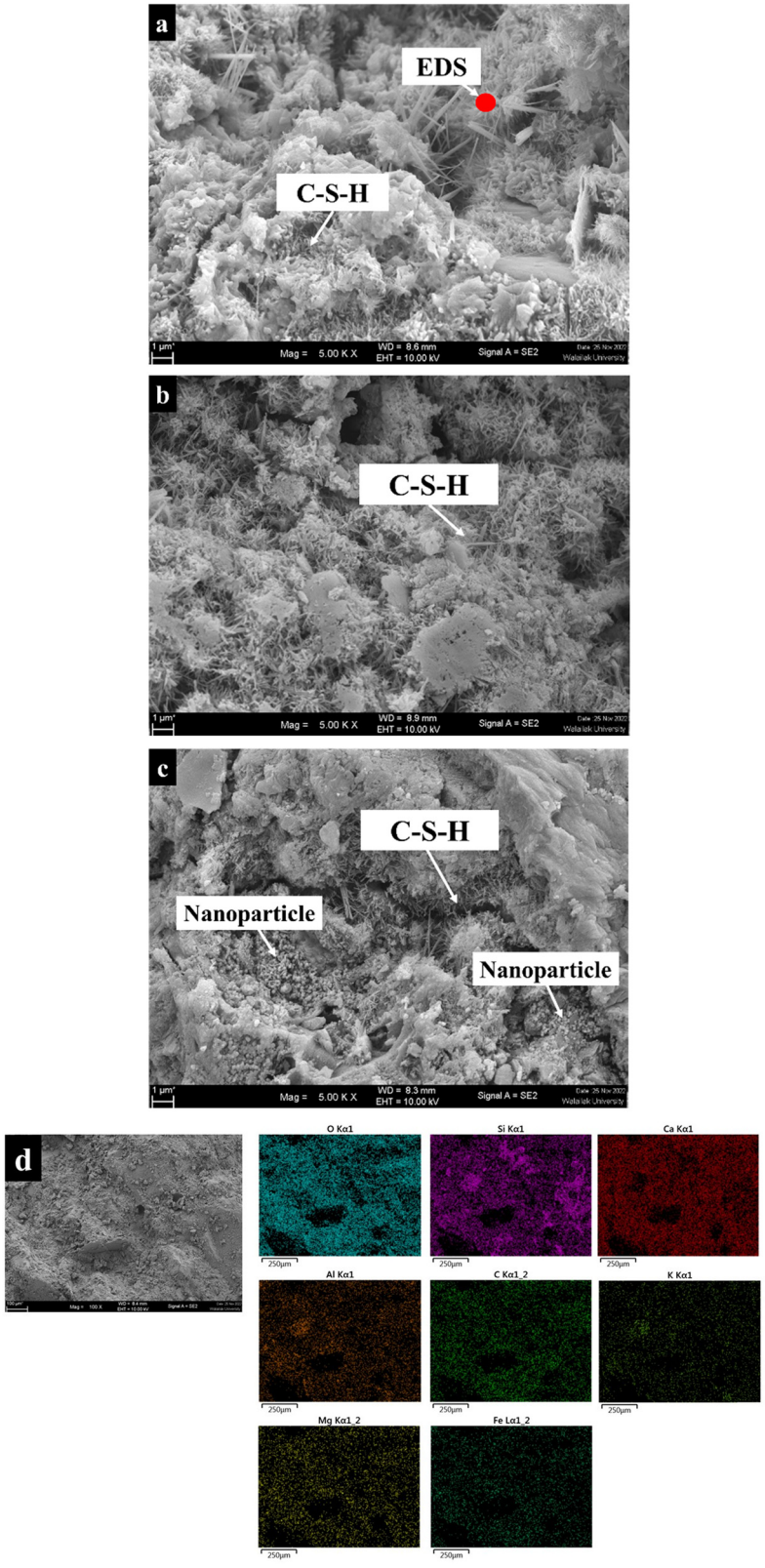

Figure 8: SEM micrographs of the 28-day samples. (a) control sample NFC0, (b) sample NFC5, (c) sample NFC10, and (d) EDS mapping of NFC5.

Table 2: Chemical analysis by SEM-EDS

Element	Weight fraction (%)	
	Red point in CT (Figure 7a)	Mapping in Figure 8
C	10.05	12.08
O	45.55	42.33
Mg	0.25	0.80
Al	2.01	2.10
Si	11.84	11.07
Ca	30.69	26.99
Fe	—	4.10
K	—	0.53

To confirm the reaction of portlandite with nano-Fe_3O_4, the crystalline size of portlandite at ≈34° 2θ was used, according to the Scherrer equation, as shown in equation (6). At this peak, the portlandite was not found at all in the samples of 7 days. The growth of portlandite crystalline at 28 days was calculated as 41.34, 37.74, and 30.14 nm for NFC0, NFC5, and NFC10, respectively. The decrease in the crystalline size of portlandite during hydration is primarily caused by its ongoing dissolution, reprecipitation, interaction with pozzolanic materials, and strain effects [42]. These processes lead to smaller, less ordered crystallites, which are reflected in the XRD pattern as broader peaks. In this work, the crystalline size of portlandite obviously decreased with the nano-Fe_3O_4 ratios. This means that the nano-Fe_3O_4 could react with portlandite or $Ca(OH)_2$ to produce more hydration products. The crystalline sizes continued decreasing to 37.74, 34.72, and 28.94 nm for NFC0, NFC5, and NFC10, respectively, when curing times were prolonged (90 days). This finding related to the development of compressive strength from early to late curing times (Figure 4)

$$D = \frac{K\lambda}{\beta \cos \theta}, \tag{6}$$

where D is the crystallite size, K is the shape factor (~0.9), λ is the wavelength of the X-ray, β is the full width at half maximum (FWHM), and θ is the Bragg angle.

The FTIR spectra of the 28-day NFC0, NFC5, and NFC10 samples are shown in Figure 7. For the purpose of this study, changes in the wavelength range 800–1,200 cm^{-1} were selected to monitor the behavior of the mixtures

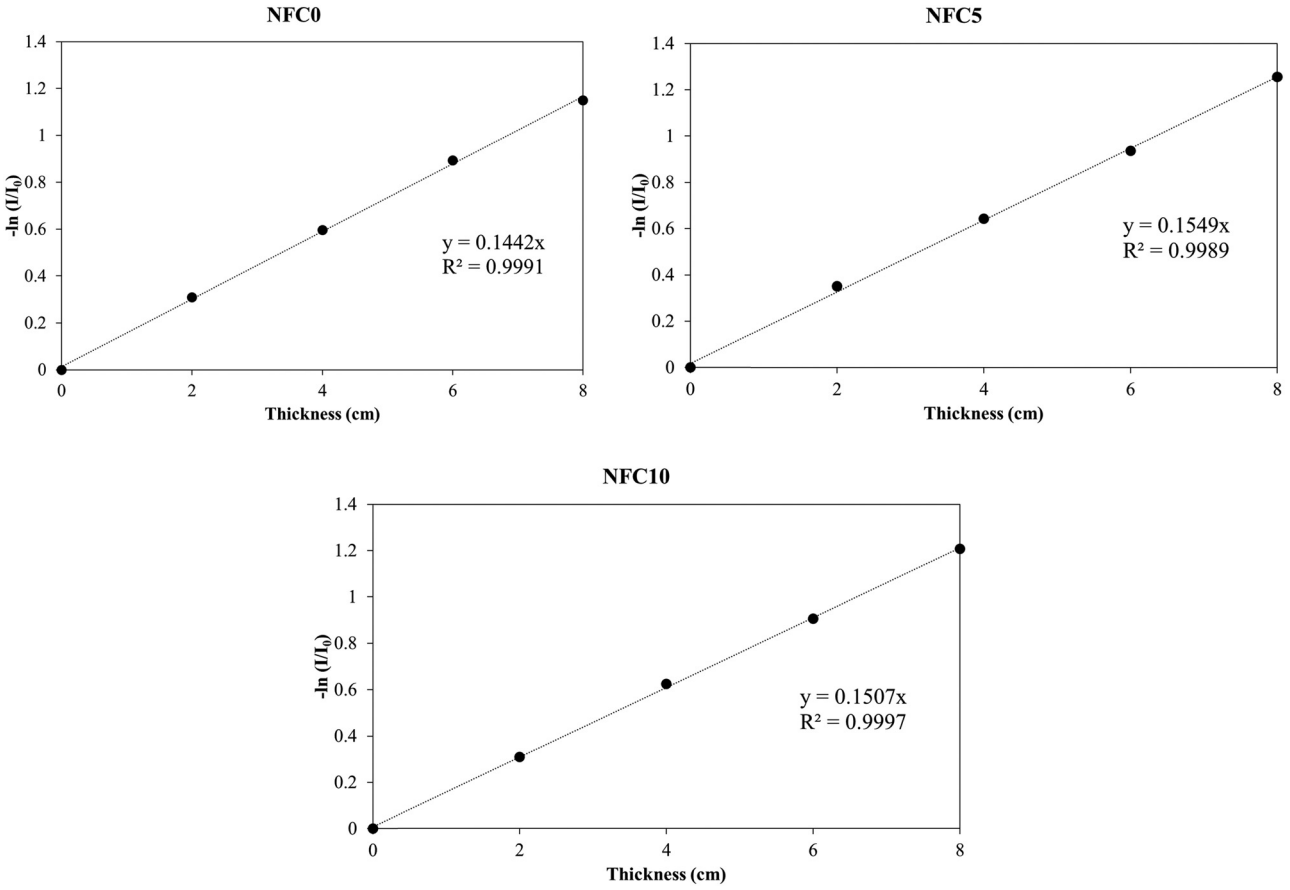

Figure 9: Relationships between $-\ln(I/I_0)$ and sample thickness for gamma-ray transmission.

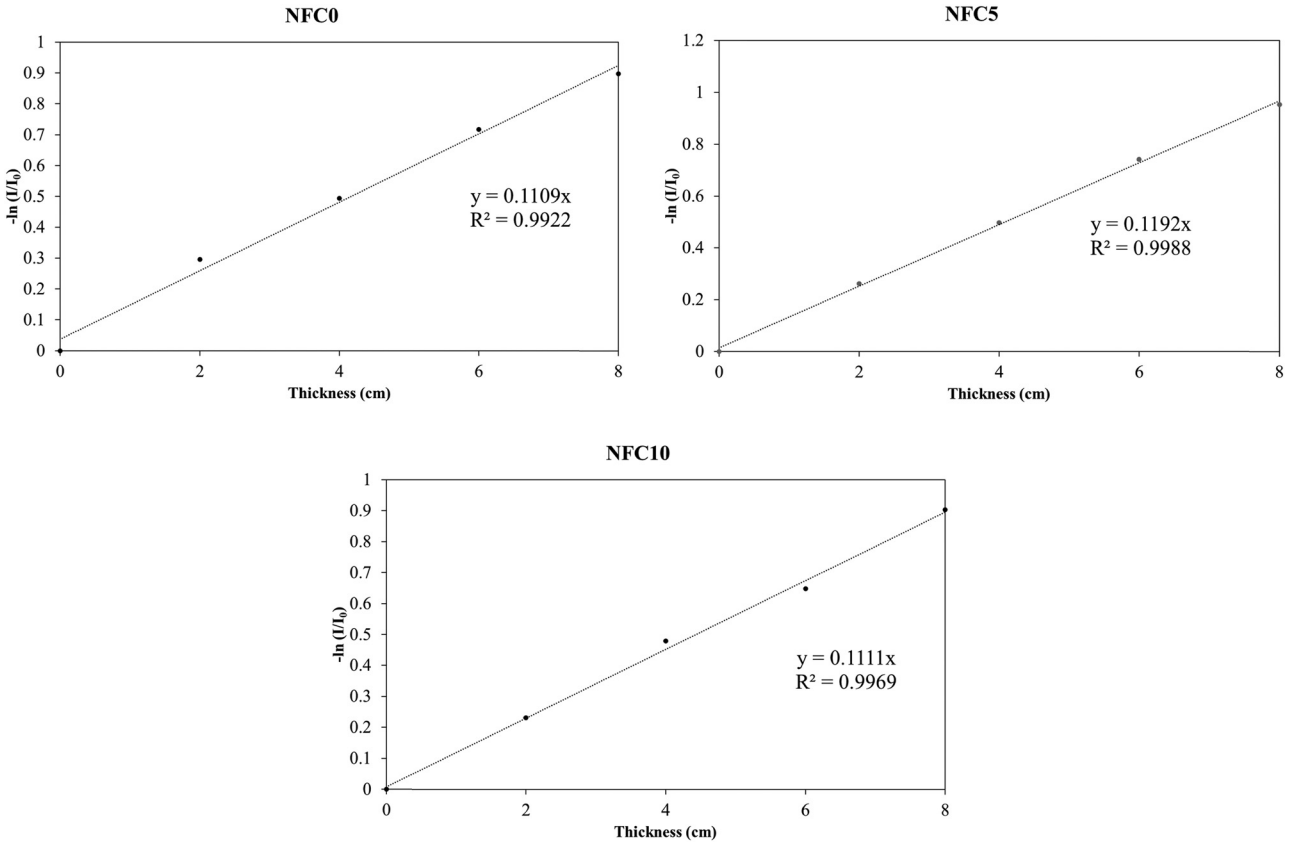

Figure 10: Relationships between $-\ln(I/I_0)$ and sample thickness for neutron transmission.

Table 3: Experimental and theoretical radiation transmission results

Parameters	NFC0	NFC5	NFC10
Gamma transmission			
Experimental			
μ (cm^{-1})	0.144	0.155	0.151
μ_m ($cm^2\ g^{-1}$)	0.083	0.086	0.086
HVL (cm)	4.807	4.475	4.600
TVL (cm)	15.968	14.865	15.279
mfp (cm)	6.935	6.456	6.636
Calculated			
μ (cm^{-1})	0.136	0.145	0.138
μ_m ($cm^2\ g^{-1}$)	0.079	0.079	0.079
HVL (cm)	5.081	4.771	5.051
TVL (cm)	16.879	15.848	16.660
mfp (cm)	7.331	6.883	7.235
Neutron transmission			
Σ_R (cm^{-1})	0.1109	0.1192	0.1119
Σ_{Rm} ($cm^2\ g^{-1}$)	0.064	0.065	0.064
HVL (cm)	6.250	5.815	6.194
TVL (cm)	20.763	19.317	20.577
mfp (cm)	9.017	8.389	8.937

containing nano-Fe_3O_4 compared with the control sample (NFC0). The peak at 969 cm^{-1} in the control is related to the polymerization of SiO_4 units during the hydration of cement [44]. The addition of nano-Fe_3O_4 shifts this peak to 1,032 and 990 cm^{-1} in samples NFC5 and NFC10, respectively (Figure 7). Previous workers have reported that the shifts in these peaks during cement hydration are indicators of the degree of polymerization of these silicate units [45–47], with a higher wavelength number corresponding to a higher degree of polymerization. Thus, the higher SiO_4 wavelengths in samples NFC5 and NFC10 compared with the control sample NFC0 indicate a greater degree of polymerization associated with the formation of C–S–H. This result is in agreement with the observed enhancement of compressive strengths in mixtures containing nano-Fe_3O_4.

The SEM micrographs of the 28-day samples NFC5, NFC10, and the control sample NFC0 are shown in Figure 8. These reveal the presence of C–S–H on the surface of all the samples, including those containing nano-Fe_3O_4. In addition, sample NFC10 (Figure 8c) is also seen to contain surface nanoparticles. At higher concentrations, the high specific surface energy of these nanoparticles can cause them to agglomerate, leading to a slight improvement in the hydration process [28,32]. This observation of surface nanoparticle agglomeration suggests an explanation for the observed reduction of the

Table 4: Chemical composition of selected magnetite/mortar samples and the control sample NFC0

Compounds	Concentration (%)		
	NFC0	NFC5	NFC10
CaO	15.47	15.30	15.14
SiO_2	59.59	58.94	58.31
Fe_2O_3	0.75	0.74	0.73
Fe_3O_4	—	1.06	2.09
Al_2O_3	4.51	4.46	4.41
MgO	0.42	0.42	0.43
Na_2O	0.34	0.34	0.34
P_2O_5	0.01	0.01	0.01
SO_3	0.97	0.96	0.96
Cl	—	—	—
TiO_2	0.08	0.08	0.08
MnO	0.01	0.01	0.02
ZnO	—	—	—
K_2O	0.61	0.61	0.60
SrO	0.02	0.02	0.02
H_2O	17.23	17.05	16.86

compressive strengths in the samples containing >5% nano-Fe_3O_4.

The chemical analysis by SEM-EDS, as shown in Table 2, represents the weight fraction of C–S–H (red point in Figure 8a) as 30.69% Ca and 11.84% Si. According to the stoichiometric ratio of C–S–H, the Ca/Si ratio ranged from 1.2 to 2.3, with a mean value of 1.7–1.8 [48,49]. In this work, the Ca/Si ratio was calculated as 1.81, which was in line with the literature. From EDS mapping of NFC5 samples (Figure 8d), the Fe was dispersed on the surface with a weight fraction of 4.10%. This value is related to the nano-Fe_3O_4 ratio used in the mixture of NFC5.

3.4 Gamma-ray and neutron transmission

Figures 9 and 10 show the relationships between $-\ln(I/I_0)$ and the sample thickness for gamma-ray and neutron transmission, respectively. The slopes of each graph with $R^2 > 0.99$ indicate the linear attenuation coefficient (μ) of photons (Figure 9) and the fast removal cross-section (Σ_R) of neutrons (Figure 10). The linear attenuation coefficient values (μ) of the gamma-rays are 0.1442, 0.1549, and 0.1507 cm^{-1} for NFC0, NFC5, and NFC10, respectively. Hassan *et al.* [50] noted that the gamma-ray shielding property of a material depends on the photon energy and the atomic number as well as the dry density of the material. For cementitious materials, gamma-ray transmission can be reduced by increasing the dry density of the cementitious material [5,12,51]. In the present work, the dry densities decreased in the order NFC5 > NFC10 > NFC0, which corresponds to the linear attenuation coefficient value (μ). Based on these values of the linear attenuation coefficients, the smallest thickness of the half-value layer HVL and tenth-value layer TVL (the sample thickness that reduces the radiation intensity to half or one-tenth of its original value, respectively) is 4.475 cm and 14.865 cm, and the mfp is 6.456 cm; these optimum values of the shielding properties are displayed by sample NFC5 (Table 3). The dense structure of sample NFC5 explains its enhanced ability to attenuate the radiation energy [51]. As further confirmation of these experimental gamma-ray results, theoretical values of μ, μ_m, HVL, TVL, and mfp were determined using Phy-X/PSD software [52] (Table 3). These calculations show good agreement between the experimental and theoretical results, with an estimated error of 5.6, 6.5, and 8.5% for samples NFC0, NFC5, and NFC10, respectively, *i.e.*, all within an error of <10% [4,53].

Table 5: Comparison of the radiation transmission results of this study with the literature

Nanomaterial	Matrix	Density (g cm^{-3})	μ (cm^{-1})	Σ_R (cm^{-1})	Ref.
5% nano-Fe_3O_4	Mortar	1.847	0.155	0.1192	This study
10% nano-Fe_3O_4	Cement paste	1.690	0.137	—	[35]
50% nano-Fe_3O_4	Cement paste	≈1.900	0.088	—	[36]
25% nano-Fe_2O_3	Mortar	2.314	0.150	—	[59]
2% nano-Fe_2O_3	Cement paste	—	≈0.173	—	[29]
2% nano-Fe_2O_3	High-density concrete	3.793	0.5568	—	[60]
1.5% nano-ZnO + 3% nano-SiO_2	High-density concrete	3.020	0.349	—	[61]
8% nano-TiO_2	Fiber-reinforced concrete	—	≈0.193	—	[62]
Control	High-density concrete	3.613	0.197*	0.013**	[56]
9% nano-TiO_2		3.649	0.229*	0.003**	
9% nano-Fe_3O_4		3.649	0.223*	0.014**	
9% nano-SiO_2		3.649	0.209*	0.013**	

Notes: *Source is ^{60}Co, 1.332 MEV, **calculated by NCNR software at 8 MeV.

Under various energies, the behaviors of the samples were also computed using Phy-X/PSD software, as shown in Table S1. All the samples showed that the values of μ decreased with increasing energy, which was in line with a previous study on RSC [54].

The trend in the values of the fast removal cross-sections (Σ_R) is similar to the linear attenuation coefficients, being 0.1109, 0.1192, and 0.1119 cm^{-1} for samples NFC0, NFC5, and NFC10, respectively. Sample NFC exhibited the highest fast removal cross-section value, but this is only slightly higher than NFC0. Cementitious materials are typically able to absorb neutrons because of their hydrogen content (approximately 1% of their unit weight) [12]. Their neutron attenuation can be improved by the addition of materials with a high neutron capture cross-section such as those containing boron, iron, or iron hydroxide [5,55]. In the present study, the addition of nano-Fe_3O_4 increased the number of iron atoms, but also resulted in the loss of H_2O (Table 4). Consequently, the addition of nano-Fe_3O_4 would have a smaller effect on neutron attenuation. However, the overall results indicate that the addition of 5% nano-Fe_3O_4 is capable of producing a radiation shielding mortar.

3.5 Comparison of the efficiency of cementitious materials containing nanomaterials

Table 5 compares the radiation transmission results (optimum density, μ and Σ_R values) of this study with the literature. All the literature indicates that gamma-ray attenuation by cementitious materials is enhanced by the presence of nanomaterials, especially in high-density concrete. This occurs by pore filling and the nucleation effects of the nanomaterials which decrease the porosity and increase the density, thereby attenuating gamma-ray shielding. Consistent with the results of the present study, the literature shows that the presence of nanomaterials has no effect on neutron attenuation (although nano-silica exhibits excellent properties in cementitious materials). Thus, the general conclusion from the literature, as well as from this study, is that nanomaterials have an excellent potential for gamma-radiation shielding cementitious materials. However, mortar or concrete for shielding applications against both gamma rays and neutrons should preferably contain more neutron absorbers [12], in addition to an optimized content of suitable nanomaterials. The latter may be based either on calculation or on experiment, but should take into account the reported negative effect of nanomaterials on neutron shielding [56]. In addition, previous research also reported that the size effect of materials became insignificant at high photon energies [57,58]. This should be further investigated in the future.

4 Conclusion

In this study, various amounts of nano-Fe_3O_4 were added to mortar for the production of radiation-shielding concrete. The physical, mechanical, microstructural, and radiation shielding properties of the resulting materials were determined with the following conclusions:

1) The addition of nano-Fe_3O_4 increased the compressive strength and dry density and decreased the water absorption by the mortar, compared to the mortar without nano-Fe_3O_4.
2) The optimum amount of added nano-Fe_3O_4 producing the best physical and mechanical properties of the mortar was 5% by weight of OPC, providing 216.79 ± 6.19 ksc at 28 days for compressive strength, 1,847 ± 19.1 kg m^{-3} for dry density, and 8% for water absorption.
3) The FTIR spectra showed that the silicate unit peak of the reference sample NFC0 at 969 cm^{-1} shifted to 1,032 and 990 cm^{-1} in the samples containing 5 and 10% nano-Fe_3O_4 (samples NFC5 and NFC10, respectively) due to the high degree of polymerization of the SiO_4 during the hydration of the OPC. This finding agreed with the XRD analysis, which exhibited the size of portlandite crystalline at 28 days calculated as 41.34, 37.74, and 30.14 nm for NFC0, NFC5, and NFC10, respectively. A smaller crystalline size refers to the dissolution and reprecipitation of portlandite crystalline to other hydration products, such as C–S–H.
4) Nano-Fe_3O_4 contents of >5% resulted in the agglomeration of the nanoparticles on the sample surface, which is related to compressive strength loss.
5) Mortars containing nano-Fe_3O_4 exhibited the potential for gamma-ray attenuation due to their greater structural density than in the control sample without nano-Fe_3O_4. By contrast, the presence of nano-Fe_3O_4 has less effect on neutron attenuation due to the influence of nano-Fe_3O_4 on the loss of H_2O from the samples.
6) The optimum values of HVL, TVL, and mfp for gamma-ray transmission by the samples were 4.475, 14.865, and 6.456 cm, respectively. The corresponding values for neutron transmission were 5.815, 19.317, and 8.389 cm^{-1}, respectively. These optimum values were for sample NFC5 (containing 5% by weight of OPC).

Acknowledgments: The authors acknowledge the instruments and laboratory support provided by the Ionizing

Radiation Metrology Section, Regulatory Technical Support Division, Office of Atoms for Peace, Ministry of Higher Education, Science, Research and Innovation, Thailand. Also, this research was supported by the National Science, Research and Innovation Fund (NSRF) and Prince of Songkla University (Grant No. ENG6601060S).

Funding information: The instruments and laboratory support were provided by Ionizing Radiation Metrology Section, Regulatory Technical Support Division, Office of Atoms for Peace, Ministry of Higher Education, Science, Research and Innovation, Thailand. Also, this research was supported by National Science, Research and Innovation Fund (NSRF) and Prince of Songkla University (Grant No. ENG6601060S).

Author contributions: All authors have accepted responsibility for the entire content of this manuscript and approved its submission.

Conflict of interest: The authors state no conflict of interest.

Data availability statement: All data generated or analyzed during this study are included in this published article.

References

[1] Mira HI, Abed NS, Tantawy HR, Tawfic AF. Mineralogical and natural radioactivity investigations of Wadi El Reddah stream sediments. Int J Environ Anal Chem. 2022;102(17):5339–55.

[2] Tawfic AF, Omar A, Abed NS, Tantawy HR. Investigation of natural radioactivity in Wadi El Reddah stream sediments and its radiological implications. Radiochemistry. 2021;63(2):243–50.

[3] Abed NS, El Feky MG, El-Taher A, Massoud EE, Khattab MR, Alqahtani MS, et al. Geochemical conditions and factors controlling the distribution of major, trace, and rare elements in sul hamed granitic rocks, Southeastern Desert, Egypt. Minerals. 2022;12(10):1245.

[4] Kunchariyakun K, Sukmak P. Utilization of garnet residue in radiation shielding cement mortar. Constr Build Mater. 2020;262:120122.

[5] Roslan MKA, Ismail M, Kueh ABH, Zin MRM. High-density concrete: Exploring Ferro boron effects in neutron and gamma radiation shielding. Constr Build Mater. 2019;215:718–25.

[6] Mann KS, Rani A, Heer MS. Shielding behaviors of some polymer and plastic materials for gamma-rays. Radiat Phys Chem. 2015;106:247–54.

[7] Kurudirek M. Radiation shielding and effective atomic number studies in different types of shielding concretes, lead base and non-lead base glass systems for total electron interaction: A comparative study. Nucl Eng Des. 2014;280:440–8.

[8] Elewa K, Belal A, El Monayeri O, Tawfic AF. Application of metal-organic framework (Zn-Ph-D CP) for copper ion removal from aqueous solution. Ain Shams Eng J. 2022;13(5):101670.

[9] Çullu M, Ertaş H. Determination of the effect of lead mine waste aggregate on some concrete properties and radiation shielding. Constr Build Mater. 2016;125:625–31.

[10] Maslehuddin M, Naqvi AA, Ibrahim M, Kalakada Z. Radiation shielding properties of concrete with electric arc furnace slag aggregates and steel shots. Ann Nucl Energy. 2013;53:192–6.

[11] Ouda AS, Abdel-Gawwad HA. The effect of replacing sand by iron slag on physical, mechanical and radiological properties of cement mortar. HBRC J. 2017;13(3):255–61.

[12] Akkurt I, El-Khayatt AM. The effect of barite proportion on neutron and gamma-ray shielding. Ann Nucl Energy. 2013;51:5–9.

[13] Micheli D, Gianola P, Bertin G, Delfini A, Pastore R, Marchetti M, et al. Electromagnetic shielding of building walls: From Roman times to the present age. IEEE Antennas Propag Mag. 2016;58(5):20–31.

[14] Abdo AE-S, Kansouh WA, Megahid RM. Investigation of radiation attenuation properties for baryte concrete. Jpn J Appl Phys. 2002;41(12R):7512.

[15] Ng JPS, Sum YL, Soong BH, Maier M, Monteiro PJM. Electromagnetic wave propagation through composite building materials in urban environments at mid-band 5G frequencies. IET Microw Antennas Propag. 2022;16(10):627–38.

[16] Pastore R, Micheli D, Vricella A, Morles RB, Marchetti M, Moglie F, et al. Advanced concrete materials for EMI reduction in protected environment and IEMI threats suppression. 2015 IEEE 15th International Conference on Environment and Electrical Engineering (EEEIC). 2015. p. 2011–6.

[17] Naus DJ, Oland CB, Ellingwood B, Mori Y, Arndt EG. Ageing management of concrete structures in nuclear power plants. Vienna: International Atomic Energy Agency; 2016.

[18] Topçu İB. Properties of heavyweight concrete produced with barite. Cem Concr Res. 2003;33(6):815–22.

[19] Tyagi G, Singhal A, Routroy S, Bhunia D, Lahoti M. Radiation shielding concrete with alternate constituents: An approach to address multiple hazards. J Hazard Mater. 2021;404:124201.

[20] International Atomic Energy Agency. Status and trends in spent fuel and radioactive waste management. Vienna: International Atomic Energy Agency; 2022.

[21] Nazari A, Riahi S. Microstructural, thermal, physical and mechanical behavior of the self compacting concrete containing SiO_2 nanoparticles. Mater Sci Eng: A. 2010;527(29):7663–72.

[22] Heikal M, Ali AI, Ismail MN, Ibrahim SANS. Behavior of composite cement pastes containing silica nano-particles at elevated temperature. Constr Build Mater. 2014;70:339–50.

[23] Sinyoung S, Kunchariyakun K, Asavapisit S, MacKenzie KJD. Synthesis of belite cement from nano-silica extracted from two rice husk ashes. J Environ Manag. 2017;190:53–60.

[24] Morsy MS, Alsayed SH, Aqel M. Hybrid effect of carbon nanotube and nano-clay on physico-mechanical properties of cement mortar. Constr Build Mater. 2011;25(1):145–9.

[25] Jalal M, Ramezanianpour AA, Pool MK. Retracted: Split tensile strength of binary blended self compacting concrete containing low volume fly ash and TiO_2 nanoparticles. Compos Part B: Eng. 2013;55:324–37.

[26] Kumari K, Preetha R, Ramachandran D, Vishwakarma V, George RP, Sundaramurthy C, et al. Nanoparticles for enhancing mechanical

properties of fly ash concrete. Mater Today: Proc. 2016;3(6):2387–93.
[27] Oltulu M, Şahin R. Effect of nano-SiO_2, nano-Al_2O_3 and nano-Fe_2O_3 powders on compressive strengths and capillary water absorption of cement mortar containing fly ash: A comparative study. Energy Build. 2013;58:292–301.
[28] Najafi Kani E, Rafiean AH, Alishah A, Hojjati Astani S, Ghaffar SH. The effects of Nano-Fe_2O_3 on the mechanical, physical and microstructure of cementitious composites. Constr Build Mater. 2021;266:121137.
[29] Abo-El-Enein SA, El-Hosiny FI, El-Gamal SMA, Amin MS, Ramadan M. Gamma radiation shielding, fire resistance and physicochemical characteristics of Portland cement pastes modified with synthesized Fe_2O_3 and ZnO nanoparticles. Constr Build Mater. 2018;173:687–706.
[30] Ji T. Preliminary study on the water permeability and microstructure of concrete incorporating nano-SiO_2. Cem Concr Res. 2005;35(10):1943–7.
[31] Amin MS, El-Gamal SMA, Hashem FS. Effect of addition of nano-magnetite on the hydration characteristics of hardened Portland cement and high slag cement pastes. J Therm Anal Calorim. 2013;112(3):1253–9.
[32] Sikora P, Horszczaruk E, Cendrowski K, Mijowska E. The influence of nano-Fe_3O_4 on the microstructure and mechanical properties of cementitious composites. Nanoscale Res Lett. 2016;11(1):182.
[33] Bragança MOGP, Portella KF, Bonato MM, Alberti E, Marino CEB. Performance of Portland cement concretes with 1% nano-Fe_3O_4 addition: Electrochemical stability under chloride and sulfate environments. Constr Build Mater. 2016;117:152–62.
[34] Sayed MSM, El-Mongy SA, Tawfic AF, Abdel-Rahman MAE. Validation of the optimized parameters for improvement of gamma spectrometers performance and efficacy. Phys Part Nucl Lett. 2021;18(2):222–31.
[35] Horszczaruk E, Brzozowski P, Sikora P, Cendrowski K, Mijowska E. The effect of nanomagnetite on the shielding properties of cementitious composites. 71st RILEM Annual Week & ICACMS 2017, Chennai, India. 2017.
[36] Florez R, Colorado HA, Alajo A, Giraldo CHC. The material characterization and gamma attenuation properties of Portland cement-Fe_3O_4 composites for potential dry cask applications. Prog Nucl Energy. 2019;111:65–73.
[37] American Society for Testing Materials. ASTM C109/C109M-20b: Standard test method for compressive strength of hydraulic cement mortars (Using 2-in. or [50 mm] Cube Specimens. West Conshohocken, PA, USA; 2020.
[38] Sikora P, Cendrowski K, Horszczaruk E, Mijowska E. The effects of Fe_3O_4 and Fe_3O_4/SiO_2 nanoparticles on the mechanical properties of cement mortars exposed to elevated temperatures. Constr Build Mater. 2018;182:441–50.
[39] Heikal M. Characteristics, textural properties and fire resistance of cement pastes containing Fe_2O_3 nano-particles. J Therm Anal Calorim. 2016;126(3):1077–87.
[40] Seifan M, Mendoza S, Berenjian A. Effect of nano and micro iron oxide particles on the workability, strength and absorption rate of cement mortar containing fly ash. Eur J Environ Civ Eng. 2022;26(9):3898–912.
[41] Zhang B, Tan H, Shen W, Xu G, Ma B, Ji X. Nano-silica and silica fume modified cement mortar used as Surface Protection Material to enhance the impermeability. Cem Concr Compos. 2018;92:7–17.
[42] Taylor HFW. Cement chemistry. 2nd edn. London: Thomas Telford Services Ltd.; 1998.
[43] Kurdowski W. Cement and concrete chemistry. Netherlands: Springer; 2014.
[44] Jose A, Nivitha MR, Krishnan JM, Robinson RG. Characterization of cement stabilized pond ash using FTIR spectroscopy. Constr Build Mater. 2020;263:120136.
[45] Ma H, Tian Y, Li Z. Interactions between organic and inorganic phases in PA- and PU/PA-modified-cement-based materials. J Mater Civ Eng. 2011;23(10):1412–21.
[46] Wongsa A, Boonserm K, Waisurasingha C, Sata V, Chindaprasirt P. Use of municipal solid waste incinerator (MSWI) bottom ash in high calcium fly ash geopolymer matrix. J Clean Prod. 2017;148:49–59.
[47] Kunchariyakun K, Sinyoung S, Kajitvichyanukul P. Comparative microstructures and mechanical properties of mortar incorporating wood fiber waste from various curing conditions. Case Stud Constr Mater. 2022;16:e00855.
[48] Pellenq RJM, Kushima A, Shahsavari R, Van Vliet KJ, Buehler MJ, Yip S, et al. A realistic molecular model of cement hydrates. Proc Natl Acad Sci. 2009;106(38):16102–7.
[49] Cuesta A, Santacruz I, De la Torre AG, Dapiaggi M, Zea-Garcia JD, Aranda MAG. Local structure and Ca/Si ratio in C-S-H gels from hydration of blends of tricalcium silicate and silica fume. Cem Concr Res. 2021;143:106405.
[50] Hassan HE, Badran HM, Aydarous A, Sharshar T. Studying the effect of nano lead compounds additives on the concrete shielding properties for γ-rays. Nucl Instrum Methods Phys Res Sect B: Beam Interact Mater At. 2015;360:81–9.
[51] Lotfi-Omran O, Sadrmomtazi A, Nikbin IM. A comprehensive study on the effect of water to cement ratio on the mechanical and radiation shielding properties of heavyweight concrete. Constr Build Mater. 2019;229:116905.
[52] Şakar E, Özpolat ÖF, Alım B, Sayyed MI, Kurudirek M. Phy-X/PSD: Development of a user friendly online software for calculation of parameters relevant to radiation shielding and dosimetry. Radiat Phys Chem. 2020;166:108496.
[53] Abd Elwahab NR, Helal N, Mohamed T, Shahin F, Ali FM. New shielding composite paste for mixed fields of fast neutrons and gamma rays. Mater Chem Phys. 2019;233:249–53.
[54] Gencel O, Bozkurt A, Kam E, Korkut T. Determination and calculation of gamma and neutron shielding characteristics of concretes containing different hematite proportions. Ann Nucl Energy. 2011;38(12):2719–23.
[55] Kharita MH, Takeyeddin M, Alnassar M, Yousef S. Development of special radiation shielding concretes using natural local materials and evaluation of their shielding characteristics. Prog Nucl Energy. 2008;50(1):33–6.
[56] Al-Tersawy SH, El-Sadany RA, Sallam HEM. Experimental gamma-ray attenuation and theoretical optimization of barite concrete mixtures with nanomaterials against neutrons and gamma rays. Constr Build Mater. 2021;289:123190.
[57] Noor Azman NZ, Siddiqui SA, Hart R, Low IM. Effect of particle size, filler loadings and x-ray tube voltage on the transmitted x-ray transmission in tungsten oxide—epoxy composites. Appl Radiat Isotopes. 2013;71(1):62–7.
[58] Noor Azman NZ, Siddiqui SA, Low IM. Characterisation of micro-sized and nano-sized tungsten oxide-epoxy composites for radiation shielding of diagnostic X-rays. Mater Sci Eng: C. 2013;33(8):4952–7.

[59] Sayyed MI, Almousa N, Elsafi M. Preparation of Mortar with Fe_2O_3 nanoparticles for radiation shielding application. Coatings. 2022;12(9):1329.
[60] Tobbala DE. Effect of Nano-ferrite addition on mechanical properties and gamma ray attenuation coefficient of steel fiber reinforced heavy weight concrete. Constr Build Mater. 2019;207:48–58.
[61] Khalaf MA, Cheah CB, Ramli M, Ahmed NM, Al-Shwaiter A. Effect of nano zinc oxide and silica on mechanical, fluid transport and radiation attenuation properties of steel furnace slag heavyweight concrete. Constr Build Mater. 2021;274:121785.
[62] Dezhampanah S, Nikbin IM, Mehdipour S, Mohebbi R, Moghadam H. Fiber- reinforced concrete containing nano - TiO_2 as a new gamma-ray radiation shielding materials. J Build Eng. 2021;44:102542.